Direct Sensitivity Based Data-Optimization Strategy for Image-Guided Diffuse Optical Tomography

Calvin B. Shaw, Zhiqiu Li, Brian W. Pogue, and Phaneendra K. Yalavarthy

***Abstract*—Implementing image-guidance for diffuse optical tomographic imaging involves reducing the spatial optical parameter space within the discrete tissue types being estimated. This makes the inverse problem overdetermined which indicates that the required number of measurements could be less than all available measurements. In this work, we propose a data-optimization approach to curtail the algorithmic complexity and implicitly reconstruct optical absorption image based on direct sensitivity approach. The performance of the proposed method was validated using numerical and gelatin phantom data indicating that this perturbation-like approach can quantify embedded regions with good accuracy and is free of bias errors associated with regularization approaches. The testing of the algorithm on human data of fast pulsatile NIR imaging in breast tissue showed that fast updates are possible and the required number of measurements is equal to discrete tissue types. The proposed method offers high level of measurement optimization for the dynamic imaging, compared to traditional methods of full iterative regularized tomography or recently proposed data resolution-based methods.**

***Index Terms*—Diffuse optical tomography, direct sensitivity, image reconstruction, measurement optimization, near infrared imaging.**

I. Introduction

DIFFUSE optical tomography is a promising non-invasive imaging modality that uses non-ionizing near-infrared (NIR) light to reveal the optical properties of the tissue under investigation [1]–[3]. The NIR light undergoes multiple scattering events inside the biological medium leading to limited spatial resolution of the reconstructed diffuse optical image [4], [5]. Several attempts have been made to improve the resolution of the reconstructed images, the most effective approach being the image-guided reconstruction, which combines the structural information obtained from traditional imaging modalities such as magnetic resonance imaging (MRI) or computed tomography (CT) with diffuse optical imaging [6], [7].

Manuscript received July 22, 2015; revised February 27, 2016; accepted April 19, 2016. This was supported by the Department of Biotechnology Innovative Young Biotechnologist Award under Grant BT/07/IYBA/2013-13. The work of C. B. Shaw was supported by the SPIE Optics and Photonics Education Scholarship.

C. B. Shaw is with the Department of Radiology and Radiological Science, Medical University of South Carolina, SC 29425 USA (e-mail: shawca@musc.edu).

P. K. Yalavarthy is with the Department of Computational and Data Sciences, Indian Institute of Science, Bangalore 560012, India (e-mail: phani@cds.iisc.ac.in).

Z. Li and B. W. Pogue are with the Thayer School of Engineering, Dartmouth College, Hanover, New Hampshire 03755 USA (e-mail: zhiqiu.li@gmail.com; brian.w.pogue@dartmouth.edu).

Color versions of one or more of the figures in this paper are available online at http://ieeexplore.ieee.org.

Digital Object Identifier 10.1109/JSTQE.2016.2558178

The image-guided reconstruction in diffuse optical imaging can be classified as *soft-prior* and *hard-prior*. The *soft-priors* approach uses the structural information in the regularization scheme to reduce the ill-posedness of the problem [7]. The *hard-priors* approach constrains the number of unknown optical properties to be reconstructed to be equal to the number of distinct tissue types which is provided by the structural imaging modalities (MRI/CT). The typical tissue types in breast imaging are essentially, adipose (fatty), fibro-glandular, and tumor region, making the number of unknown optical parameters to three [8], [9]. This reduction in the number of optical properties and guiding the solution via structural information to improve the resolution of diffuse optical images makes it a computationally efficient approach [10].

Optimization of data-collection strategy has been an active area of research, where the focus is on reducing the number of sources and detectors used for data-acquisition. A singular value analysis of the weight matrix was proposed to predict optimal data collection strategy [11], [12]. A Cramer-Rao lower bounds was investigated for diffuse optical imaging to perform data-optimization with an advantage of estimating the optical parameters without solving the inverse problems [13]. In recent works proposed for optimized data-acquisition in image-guided diffuse optical tomography includes a data-resolution matrix based approach for obtaining independent source-detector map, where the number of required detectors was reduced from 240 to 6 [14]. The crucial step in data-resolution matrix was to build a sensitivity (Jacobian) matrix, which describes a relationship between the variation of the measured flux on the boundary and the variation of the absorption inside the object under investigation [14], [15] and estimate a data resolution matrix. Although these methods have been effective, the prediction of independent source-detector map requires usage of regularization parameter as the Jacobian matrix is ill-conditioned. Hence, there is a need to develop computational methods which are free of tuning parameters in order to estimate the optimized source-detector locations in an automated fashion.

In order to overcome these shortcomings of earlier study [14], this work focuses on introducing a direct sensitivity matrix (DSM) approach, which is a simple, efficient, and regularization-free scheme to estimate the small variations in the optical absorption parameter using a perturbation like approach. In addition, the DSM scheme is used to identify the best signal-to-noise ratio measurements out of the available measurements in order to optimize the data-collection in turn reducing the required number of sources and detectors compared to the traditional schemes. The DSM approach was inspired by the application in electrical impedance tomography (EIT) to estimate

the distribution of conductivity [16], [17]. The application of DSM to EIT was limited to show the efficacy of parameter estimation without the need to invert a matrix, but in this work we extend this scheme to optimize the data-collection strategy. The objective of DSM is to obtain an approximate inversion of the sensitivity matrix without the need to directly invert it, which typically demands a regularization parameter. The performance of the proposed scheme was evaluated using a numerical patient mesh, gelatin phantom data, and a real human breast data and compared with the recently proposed data-resolution method [14] and the standard approach, which was used as a reference for comparison (human breast data). The results show that the proposed DSM scheme requires only one source-detector pair for every tissue-region defined in the mesh. Further, the DSM scheme was found to be useful in estimating small changes (temporal variations) in a dynamic imaging scenario (for real human breast data), where the scheme outperformed the existing methods in terms of reducing the number of sources-detectors as well as the reconstruction time. The effectiveness of the proposed scheme was demonstrated using a realistic numerical patient mesh where different target (tumor) locations were considered. In addition, a numerical example was considerd to show the minimal role of reduced scattering coefficient (μ_s') in the DSM in comparison with other existing methods. In order to evaluate the performance in a realistic imaging scenarios, a gelatin phantom and a real human breast data were used to show the applicability of the DSM scheme in terms of optimizing the data-acquisition procedure.

II. Methods

A. Image Guided-Diffuse Optical Tomography—Forward Problem

The continuous-wave (CW) NIR light propagation in thick biological tissue like breast can be modeled the using diffusion equation (DE) [6], given as,

$$-\nabla \cdot D(r)\nabla\Phi(r) + \mu_a(r)\Phi(r) = Q_o(r) \tag{1}$$

where $\Phi(r)$ and $Q_o(r)$ are the photon fluence and isotropic light source at a given position, r. The optical absorption parameter to be estimated is denoted as $\mu_a(r)$ (units of mm^{-1}) and $D(r)$ denotes the optical diffusion coefficient where $D(r) = \frac{1}{[3(\mu_a+\mu_s')]}$ with μ_s' representing the reduced scattering coefficient (in mm^{-1}). In this work, a finite-element based method was employed to solve the DE along with a Robin type (or Type-III) boundary condition that accounts for the refractive-index (RI) mismatch [6], [18] that is described in the following equation

$$\Phi(\xi) + 2A\hat{n}\cdot D(\xi)\nabla\Phi(\xi) = 0 \tag{2}$$

where ξ and $\hat{n}$ are represent a point on the external boundary and an outward pointing normal respectively, and A is a factor that depends upon the relative refractive index mismatch between the tissue domain (Ω) and air. The factor A can be derived from the Fresnel' law:

$$A = \frac{2/(1-R_0) - 1 + |\cos\theta_c|^3}{1 - |\cos\theta_c|^2} \tag{3}$$

where $\theta_c = \arcsin(n_{air}/n_1)$ represents the angle at which total internal reflection occurs for photons traveling from region Ω with RI n_1 to air having RI n_{air}, and $R_0 = (n_1/n_{air} - 1)^2/(n_1/n_{air}+1)^2$. The source condition is assumed to be spherically isotropic and is centered one transport scattering distance $(1/\mu_s')$ within the outer boundary, $\delta\Omega$. The sampled version of $\Phi(r)$ at detector locations for the continuous wave system is the natural logarithm of the intensity, represented as $Y^C(\mu_a)$.

B. Image Guided-Diffuse Optical Tomography—Inverse Problem

The unknown optical absorption parameter (μ_a) in each region is estimated iteratively by matching the experimental boundary data (Y^E) and the computed data ($Y^C(\mu_a)$) in the least square sense [8]. The objective function to be minimized with respect to μ_a in this case is,

$$\Omega(\mu_a) = ||Y^E - Y^C(\mu_a)||_2^2. \tag{4}$$

In here, the dimension of μ_a is $R \times 1$, where R represents the number of regions and $Y^{E/C}$ has a dimension of $M \times 1$, where M represents the number of measurements which is typically given by the product of number of sources (S) and detectors (D) used in the imaging setup. The Levenberg Marquardt (LM) minimization scheme is typically adapted to solve the above objective function, which results in the following iterative update equation [8]

$$[\mathbf{J}^{\mathbf{T}}_{(\mathbf{k-1})}\mathbf{J}_{(\mathbf{k-1})} + \lambda\mathbf{I}]\triangle\mu_a^k = \mathbf{J}_{(\mathbf{k-1})}[Y^E - Y^C(\mu_a^{(k-1)})] \tag{5}$$

where, k represents the update at k'th iteration and $\mathbf{J}$, is the Jacobian/sensitivity matrix where $\mathbf{J} = \frac{\partial Y^C(\mu_a)}{\partial \mu_a}$ with a dimension of $M \times R$. In here, $\mathbf{I}$ is the identity matrix and λ is the regularization parameter. In the LM scheme, λ is monotonically decreased after each iteration by a factor (in this work, $10^{0.25}$) and this procedure is repeated until the change in the objective function (Ω) in successive iteration becomes less than 2% [8]. At the end of each iteration, the μ_a is updated with $\triangle\mu_a$, and subsequently recalculating the $\mathbf{J}$ matrix and the computed data, $Y^C(\mu_a)$ to estimate the next iterate. Note that although $R \ll M$, the $\mathbf{J}$ matrix can still be ill-conditioned which results in the use of regularization parameter (λ) [19], [20]. The convergence properties of the LM scheme is governed by this regularization parameter and as a result an optimal choice is crucial to effectively estimate μ_a. The LM scheme will be identified as the "standard" method for all the results presented in this study and it is important to note that this method utilizes all the source-detector pairs for data-acquisition and reconstruction and in turn serves as a reference model where the ground truth is not available.

1) Data-Resolution Approach: In a recent work [14], a data-resolution matrix based approach was proposed for image guided diffuse optical tomography which demonstrated the ability to reduce the number of required measurements compared to the standard method without compromising the reconstruction performance. The independent measurement selection

is made based on the data-resolution matrix given by

$$\mathbf{N} = \mathbf{J}[\mathbf{J^T J} + \lambda \mathbf{I}]^{-1}\mathbf{J^T} \tag{6}$$

where $\mathbf{J}$ is the Jacobian matrix as discussed earlier and λ is the regularization parameter. The independent measurements were chosen based on the magnitude of the diagonal values of the data-resolution matrix, which reveal the significance of a particular measurement and the off-diagonal values relating the dependence among measurements [14], [15]. In order to decide the optimal minimal measurements, the matrix $\mathbf{N}$ is computed at the first iteration followed by sorting the diagonal entries of $\mathbf{N}$ in the descending order to reveal the importance of a particular measurement. Now, the optimal choice is made based on picking the first few entries of the sorted diagonal entries as the first entry is important and like-wise the last entry being least important. The threshold to pick the diagonal entries was made based on the condition number of the reduced matrix $\mathbf{J}$ and after a thorough analysis this optimal value was found to be 6 (see Ref. [14] for further details). In other words, the first six sorted diagonal entries were considered to pick the optimal source-detector pairs.

In the approach discussed above, the data-resolution approach does not depend on the specific measurement (Y^E) but depends on how many diagonal entries are considered and the regularization parameter (λ) that is used to construct the matrix, $\mathbf{N}$. As a result a heuristic selection of these parameters may result in a sub-optimal estimation of the independent source-detector locations. In order to overcome this limitation, it would be beneficial to come up with optimization schemes that is automated, which can predict the optimal source-detector map without any user-defined parameters. Moreover, any efficient scheme that can reduce the number of required measurements from 'M' to 'R' will increase the speed of data-acquisition and the aim of direct sensitivity approach (proposed here) will enable this.

2) Direct Sensitivity Matrix (DSM) Approach: The first step in the DSM approach is to establish a relationship between the experimental data (Y^E) and the unknown optical absorption parameter (μ_a), which can be expressed as [16]:

$$\mu_{ai} = f_i(y_1^E, y_2^E, \ldots, y_M^E). \tag{7}$$

Assuming f_i relates the two quantities, μ_a and Y^E with $i = 1$ to R, expanding the above relation using a Taylor series expansion around a known initial guess Y_0^C (obtained from calibration procedure) , we have

$$\mu_{ai} = f_i(Y_0^C) + f_i^{'}(Y_0^C)(Y^E - Y_0^C) + O((Y^E - Y_0^C))^2, \tag{8}$$

where $Y_0^C = (y_{1,0}^C, y_{2,0}^C, \ldots, y_{M,0}^C)$ are the computed boundary measurements corresponding to the homogeneous (initial guess) optical absorption parameter (μ_{a0}), given as

$$\mu_{a0} = f_i(Y_0^C), \tag{9}$$

where $\delta Y = Y^E - Y_0^C$ and further, linearizing leads to the higher order terms in Eq. (8) to be ignored resulting in the following relation:

$$\delta\mu_{ai} = \mu_{ai} - \mu_{a0} = f_i^{'}(Y_0^C)\delta Y = \sum_{j=1}^{M} d_{ij}\delta Y \tag{10}$$

where $f_i^{'}(Y_0^C) = d_i = [d_{i,1}, d_{i,2}, \ldots, d_{i,M}] = [\frac{\partial\mu_{ai}}{\partial y_1}|_{y_1 = y_{1,0}^C}, \frac{\partial\mu_{ai}}{\partial y_2}|_{y_2 = y_{2,0}^C}, \ldots, \frac{\partial\mu_{ai}}{\partial y_M}|_{y_M = y_{M,0}^C}]$ with d_{ij} representing the direct sensitivity coefficients (DSC's), which is used to estimate $\delta\mu_a$ from δY.

The nodal values ($\delta\mu_{ai}$) are normalized in practice to get a dimensionless quantity [16], [17], defined by

$$\delta\mu_{ai} = \left[\sum_{j=1}^{M} d_{i,j}\delta y_j\right]\left[\sum_{j=1}^{M} d_{i,j}y_{j,0}^C\right]^{-1}. \tag{11}$$

As the function f_i is unknown, calculating $d_{i,j}$ is analytically not possible as a result, the following numerical approximation is made [16], [17]:

$$\partial\mu_{ai}/\partial y_j \approx \delta\mu_{ai}/\delta y_j. \tag{12}$$

Now the calculation of direct sensitivity coefficients ($d_{i,j}$) is achieved using the finite element method (FEM) [8], [18]. It is worth noting that the above procedure is similar to the perturbation approach to calculate $\mathbf{J}$ except that the inversion is avoided by calculating the sensitivity coefficients directly and this procedure is repeated until the change in the objective function ($\Omega(\mu_a)$, Eq. (2)) in successive iteration becomes less than 2% [8].

It is important to note that the reconstructed value of each nodal absorption parameter ($\delta\mu_{ai}$) in Eq. (10) is simply an inner product between the computed direct sensitivity coefficients of each node and the fluence measurements. But, the magnitudes of DSC's are not uniform as a result it may give more weight to a certain node than others which can happen if the quantity, δY is close to zero [16]. In order to avoid such numerical instabilities, the smallest d_i is chosen (i.e., ind $= \min[d_{i,1}, d_{i,2}, \ldots, d_{i,M}]$) which in turn indicates the direct sensitivity coefficient with the best signal-to-noise ratio (see Ref. [16] for a detailed explanation). Further, the index (ind) with the largest signal-to-noise ratio is in turn used to identify the source-detector pair for each region. This step to compute the indices (ind) was performed at the first iteration and the subsequent iterations use the same source-detector pair to compute the absorption coefficient (μ_a) for each region. This measurement selection reduces the required number of measurements from 'M' to 'R' making the proposed scheme highly optimized and parameter-free in order to choose the independent measurement indices as opposed to the data-resolution approach.

For all the computations performed here, a Linux workstation with 2.4 GHz Intel Quadcore processor and 8 GB RAM was used. For solving the NIR-light propagation forward problem, MATLAB-based open-source (NIRFAST) toolbox [18] was used.

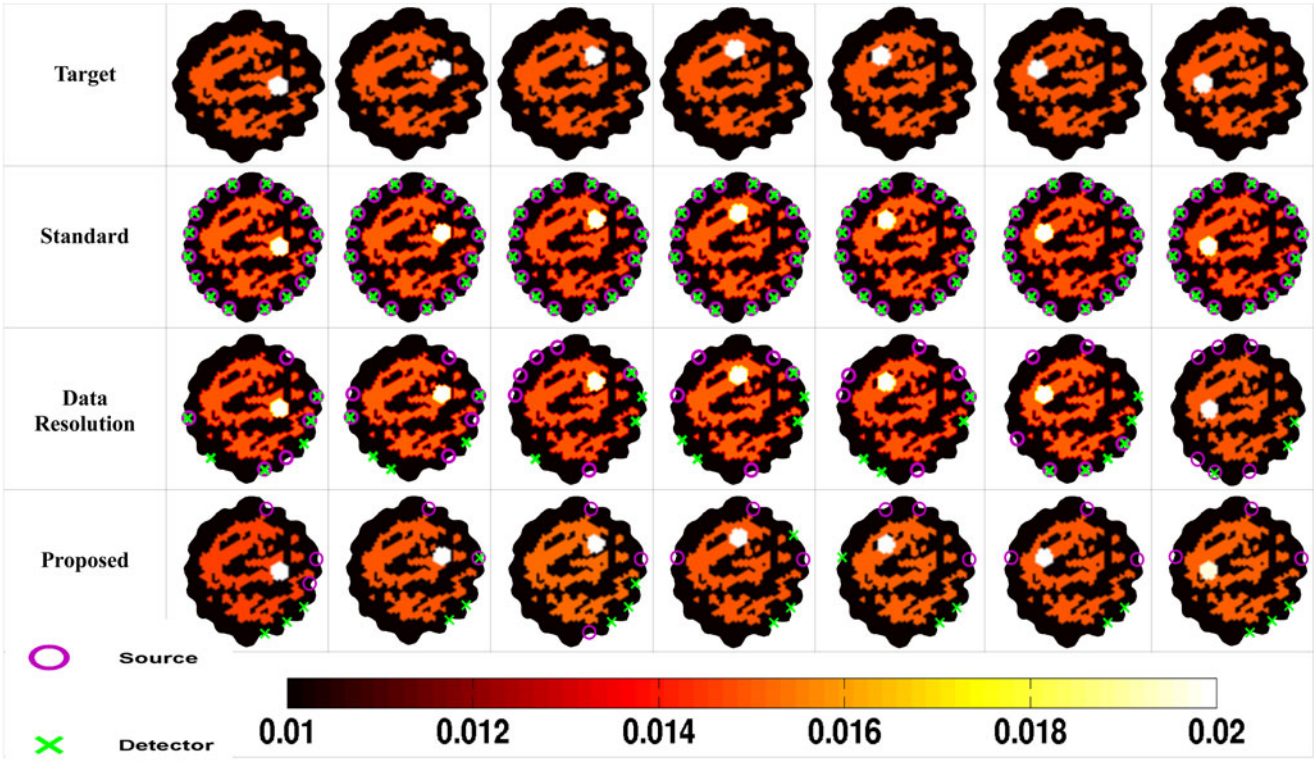

Fig. 1. Comparison of the μ_a reconstruction distribution using the standard, data resolution, and proposed methods for the case of patient mimicking numerical experiment. The target distribution is given in the first row for seven different target locations. The numerically generated data was corrupted with 1% normally distributed Gaussian noise. The corresponding sources (circles) and detectors (cross marks) for each case are also indicated along the boundary of each reconstructed image.

III. Simulation and Experimental Evaluation

A. Patient Mimicking Numerical Experiment

To evaluate the effectiveness of the proposed scheme with other discussed schemes, a patient mimicking irregular mesh was considered, where the geometry was acquired at Dartmouth NIR-MRI setup. The breast tissue morphology captured by the MRI setup consisted of both fatty and fibro-glandular (fibrous) tissue. Two distinct optical absorption values (μ_a) were considered for each of the tissue region in which the fatty and fibrous regions were set to 0.01 mm^{-1} and 0.015 mm^{-1} respectively. In order to check for the robustness of the methods discussed in this work, seven different cases were considered in which a third circular region mimicking a tumor was placed in seven different locations where the starting position was placed on x-axis (20, 0) and was placed in different locations to reach diagonally opposite location $(-20, 0)$. The target distribution for the seven different cases is given in the first row of Fig. 1 where the target region had an absorption value of 0.02 mm^{-1}, and with a radius of 7.5 mm. As the measurement setup considered in this work was in continuous-wave domain, the reduced scattering coefficient (μ_s') and the refractive index were set to 1 mm^{-1} and 1.33 throughout the domain.

The data-collection system had 16 fibers arranged in a circular fashion, wherein when one fiber acted as a source (placed at one mean transport length inside the boundary), the rest acted as detectors amounting to $16 \times 15 = 240$ number of measurements (M). The sources considered in the imaging setup had Gaussian profiles with a full-width at half maximum (FWHM) of 3 mm to replicate the realistic experimental scenario. The numerical data was generated on a fine mesh containing 10 249 nodes which corresponds to 20 160 triangular elements, further a normally distributed Gaussian noise of 1% was added to the measured data. The standard case used all the 240 measurements while the data-resolution and the proposed scheme utilized only subset of available measurements to estimate the absorption parameters for each region in the imaging domain.

B. Gelatin Phantom Experiment

An experimental validation using a gelatin phantom was carried out to demonstrate the efficacy of the proposed scheme and was in turn compared with two existing methods discussed for image guided diffuse optical tomographic image reconstruction. The gelatin cylindrical phantom was of height 25 mm and diameter 86 mm imitating a realistic breast tissue was considered. The phantom was made up of mixture containing Titanium oxide (TiO_2) and India ink to obtain the effect of scattering and absorption respectively [8]. The gelatin phantom consisted of three different layers mimicking the adipose, fibrous, and tumor region which were formed by hardening heated gelatin solution (80% of deionized water and 20% of gelatin). The optical properties of the outer-most region (adipose) with a thickness of 10 mm were $\mu_a = 0.0065$ mm^{-1} and $\mu_s' = 0.65$ mm^{-1}.

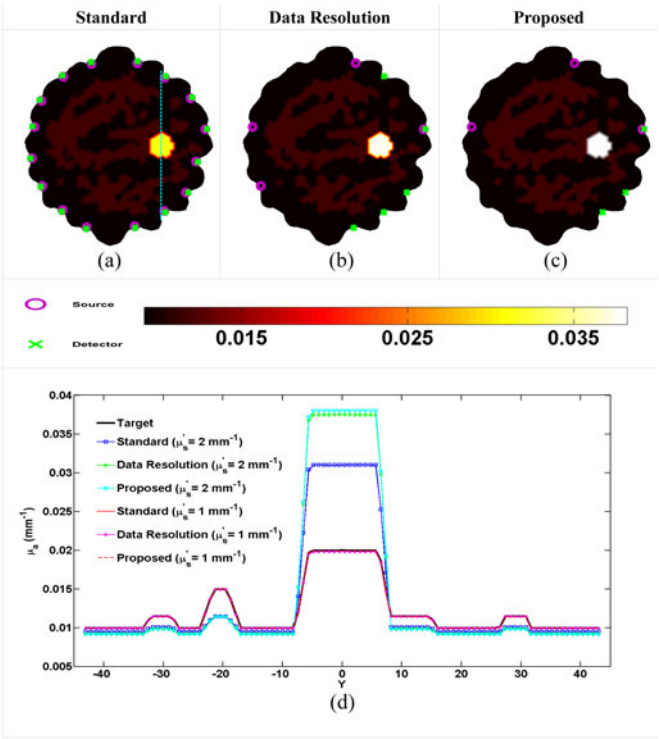

Fig. 2. A numerical example illustrating the effect of μ_s' on the reconstruction methods in which μ_s' of the tumor (target) in the first example (case considered in column-2 of Fig. 1) was increased from 1 mm^{-1} to 2 mm^{-1} . (d). The one-dimensional cross-sectional plot along the dashed line given in the image (a) for the reconstructed images given in (a)–(c) for the case $\mu_s' = 2$ mm^{-1} as well as the reconstructed images in the second column of Fig. 1 for the case $\mu_s' = 1$ mm^{-1}. The corresponding sources (circles) and detectors (cross marks) for each case are also indicated along the boundary of each reconstructed image.

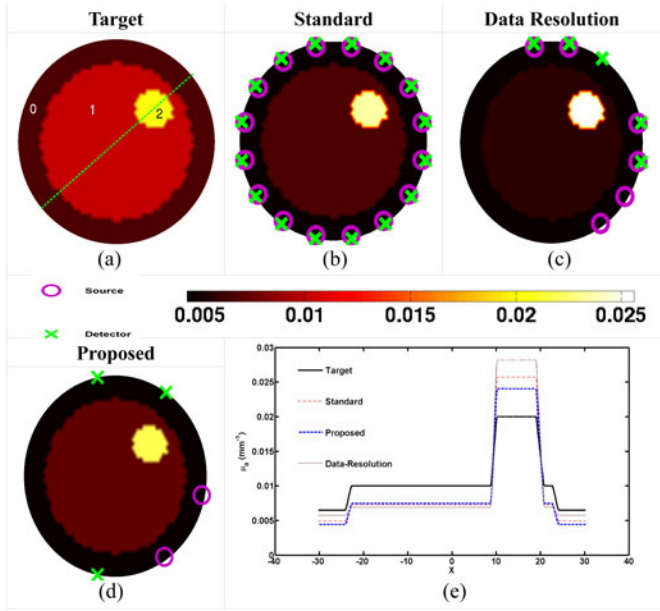

Fig. 3. Reconstructed μ_a distributions using (b) standard, (c) data resolution, and (d) proposed methods described in this work for the experimental gelatin phantom case with the target image given in (a). (e). The one-dimensional cross-sectional plot along the dashed line given in the target image (a) for the reconstructed images given in (b)–(d). The corresponding sources (circles) and detectors (cross marks) for each case are also indicated along the boundary of each reconstructed image.

The middle layer (fibrous) with a diameter of 76 mm had $\mu_a = 0.01$ mm^{-1} and $\mu_s' = 1$ mm^{-1}. Lastly, the third region (mimicking tumor) with a radius of 8 mm had $\mu_a = 0.02$ mm^{-1} and $\mu_s' = 2$ mm^{-1}. The data was acquired at the Dartmouth-NIR system at a wavelength of 785 nm [8] and a mesh consisting of 1785 nodes corresponding to 3418 elements was used for the reconstruction purpose. The two-dimensional cross-section of the phantom is shown in Fig. 3(a).

C. Human Breast Data

In the third case a real human breast data was considered. A near-infrared tomography system with spectral encoded sources using the guidance from magnetic resonance imaging was considered. This data was an initial human study to effectively quantify the small-scale pulsatile changes of hemoglobin within the human breast [21]. This system along with an MR-compatible on-line finger pulse oximeter (PO) plethysmogram (Veris Vital Signs Monitor, MEDRAD, Inc.) was incorporated into an MR scanner. The subject was simultaneously imaged by the MR and NIR system and for the phase reference, the PO was clamped to the subject's finger. A total of seven NIR 785 nm single mode laser diode sources were used to image the subject and the NIR system acquired the data at 10 Hz resulting in a 275 s data set and the MR scan taking 15 min to obtain the T1- and T2-weighted coronal images of the breast [21]. The corresponding coronal T1-weighted image is shown in Fig. 4(a) where the darker regions represent the fibroglandular region with higher hemoglobin content and the lighter regions represent the fatty/ adipose region with a relatively less hemoglobin content.

A two-dimensional mesh with 8000 nodes was considered for the reconstruction purpose, which was segmented into fibroglandular and adipose regions, based on the MR-image (given in Fig. 4(b)). The NIR system had seven laser diode sources and seven detectors placed opposite each other resulting in a total of 49 measurements which was in turn used to carry out the region-based reconstruction. The optical scattering coefficients (μ_s') were assumed to be 0.6 mm^{-1} and 1 mm^{-1} in the adipose and fibroglandular regions respectively. The initial guess for the optical absorption parameter (μ_a) in the mesh was assumed to be 0.006 mm^{-1}.

In Ref. [21], the relationship between the NIR signal and the pulse oximeter plethysmogram signal was reported, which was used as a frequency reference, where a 0.1 s temporal delay of absorption pulse was found in the adipose region relative to the fibroglandular region. This study showed that the signal of blood flow in the breast tissue had a strong peak from 1.1 to 1.4 Hz frequency and eventually the PO signal also shared the same peak revealing the fact that the blood flow in the breast was directly oscillating from the heart beat signal [21]. In our work, this real human data-set was used to evaluate the robustness and accuracy of the proposed scheme to quantify the small-scale pulsatile variations of hemoglobin inside the human breast. The

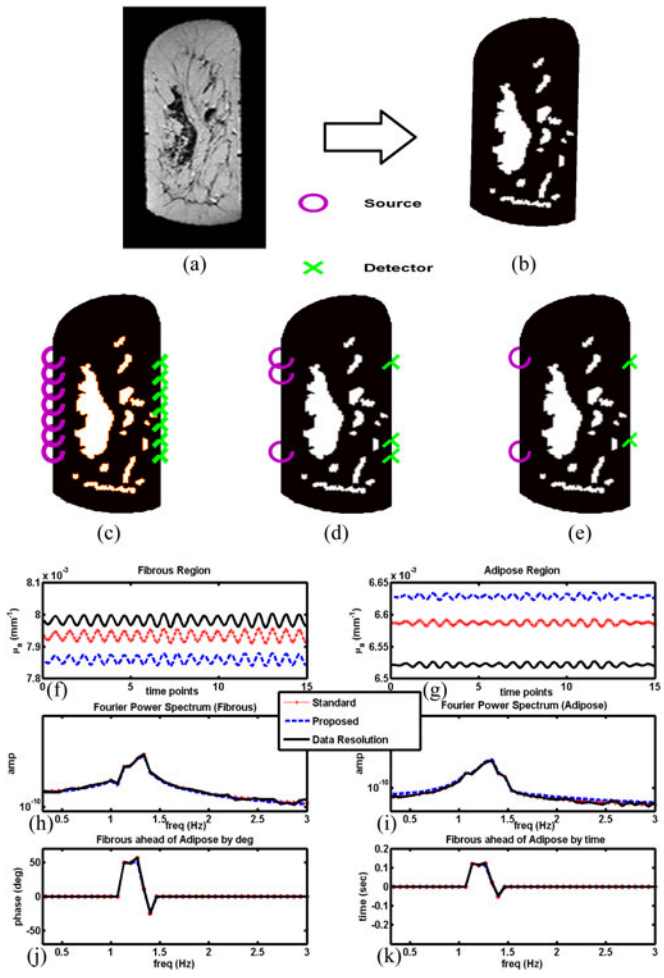

Fig. 4. (a). Coronal T1 MR image of the human breast. (b). A segmented (fibrous (white), and adipose (black)) finite element mesh. Reconstructed images with its corresponding source-detector pairs for (c) standard, (d) data resolution, and (e) proposed schemes. Reconstructed μ_a values using the various reconstruction methods in (f) the fibroglandular region and the (g) adipose region for the human breast data. (h) The Fourier power spectrum of the reconstructed μ_a values in the fibroglandular region and (i) in the adipose region. (j) A plot of the phase difference of μ_a between the fibroglandular and the adipose region versus frequency and (k) the time delay (temporal translation of phase) between the two regions versus frequency.

obtained results using the proposed scheme along with data resolution were compared with the standard scheme, which was used as a reference to observe the strong peak from 1.1 to 1.4 Hz frequency range, and a stable phase difference of approximately 50 degrees offset equivalent to a 0.1 s of temporal delay between the adipose and fibroglandular region.

IV. Results

For the case of patient mimicking numerical experiment with 1% Gaussian noise, the reconstruction results for seven different target locations are given in Fig. 1. The first row corresponds to the target distribution consisting of three distinct tissue regions namely, fatty, fibrous, and tumor regions with increasing absorption values as depicted by the color bar in the last row. Second row corresponds to the results obtained using the standard method with all the 240 measurements. The sources and detectors used for the forward and inverse model are indicated using a circular (magenta) and cross (green) symbols along the boundary of the mesh. Similarly, the third and fourth rows correspond to the results obtained using data-resolution and the proposed approaches with the optimized source-detector positions used for the forward and inverse model are indicated along the boundary of the reconstructed images. The different target locations were primarily chosen to check if the required number of measurements increased with different target locations. The regularization parameter (λ) was kept at 1.5 for all the seven cases in both the standard and data resolution approaches as this value yielded optimal results. In here, M (minimal measurements) was chosen as 6 for the data resolution matrix which turned out to be optimal while the proposed scheme resulted in 3 minimal measurements (1 source-detector pair for each region) with standard case utilizing 240 measurements.

In order to evaluate the effect of reduced scattering coefficient (μ_s') in the proposed method as well as the standard and data-resolution methods, a numerical example was considered in which the μ_s' of the tumor (target) in the first example (case considered in column-2 of Fig. 1) was increased from 1 mm^{-1} to 2 mm^{-1}. All other simulation and reconstruction parameters were kept intact similar to the cases in Fig. 1 including the noise level. The reconstructed μ_a distributions for the standard, data resolution and proposed methods are given in Fig. 2(a), (b), and (c) and the corresponding optimized source-detectors for each method is highlighted at the boundary of the reconstructed images. Fig 2(d) shows the one-dimensional cross sectional plot along the dashed line shown in Fig. 2(a) for the reconstructed images given in Fig. 2(a)–(c) for the case $\mu_s' = 2$ mm^{-1} as well as the reconstructed images in the second column of Fig. 1 for the case $\mu_s' = 1$ mm^{-1} . A change in the reduced scattering coefficient, indeed affects the SNR measured by each detector, as a result the locations of the sources and detectors vary in the two presented cases. In addition, it is worth noting that the estimated μ_a values were over-estimated for the case $\mu_s' = 2$ mm^{-1} compared to $\mu_s' = 1$ mm^{-1}.

The reconstruction results obtained for the gelatin phantom data using the standard, data resolution, and the proposed schemes are shown in Fig. 3(b), (c), and (d) respectively. The target distribution is shown in Fig. 3(a) with regions labeled as '0', '1' and '2' representing the fatty, fibrous, and tumor mimicking regions respectively and the line-profile plot along the dashed line in the target image for various reconstruction methods are given in Fig. 3(e). Similar to the earlier case, the source-detector positions are indicated along the boundary of the each reconstructed images to show how many source-detector pairs were required by each of the discussed schemes. The regularization parameter for this case was set to 0.01 as this was the value used even in the previous study to compare the data resolution approach with the standard method [14]. Even in this case, the minimal measurements was chosen as 6 for the data resolution matrix which turned out to be optimal while the proposed scheme resulted in 3 minimal measurements with standard case utilizing 240 measurements.

The reconstruction results pertaining to the human breast data case is given in Fig. 4. The coronal section of the T1-weighted image MR image of the human breast is given in (a). The segmented image obtained from T1-weighted image is shown in (b) with the fibrous region represented by the white segment and adipose by the black segment. Second row shows the reconstructed images obtained using the (c) standard, (d) data resolution, and (e) proposed methods with optimal source-detector pairs for each method is given along the boundary of the reconstructed image. Fig. 4(f) and (g) show the first 15 s of reconstructed optical absorption (μ_a) values in the fibrous and adipose regions respectively using the standard, proposed, and data resolution methods. Similarly, Fig. 4(h) and (i) show the Fourier power spectrum of the two regions, Fig. 4(j) shows the plot of phase difference of μ_a between the fibroglandular and the adipose regions with respect to frequency and finally Fig. 4(k) shows the temporal variation (translation of phase to time) of μ_a in the two regions versus frequency. The parameter, λ was set to 0.1 in this case for standard and data resolution methods. The optimal measurements for the data resolution case was found to be 4 while the direct-sensitivity (proposed) approach required only 2 measurements to estimate the absorption values.

V. Discussion

The direct sensitivity approach has been utilized for electrical impedance tomography before, but this method was only utilized to identify the best signal-to-noise-ratio data points using a perturbation like approach to reconstruct the conductivity of the imaging domain. In this work, we extend this approach not only to identify the effective signal-to-noise-ratio data points, but additionally to utilize this information to optimize the data-collection procedure for image-guided diffuse optical tomography. It is worth highlighting that the reconstruction procedure adapted in this work eliminates the need to construct a DSM (Eq. (11)) unlike the standard and data-resolution approaches which demand the need to construct the Jacobian/ sensitivity matrix followed by an inversion. Further more, the proposed direct sensitivity approach is a parameter free procedure to estimate the optical absorption (μ_a) for the distinct regions associated with the tissue unlike the standard and data resolution approaches which typically require a regularization parameter (λ) (Eqs. (5) and (6)). We observed that a sub-optimal λ lead to aberrant results where the reconstructed image completely missed the target region and the resulting μ_a had only the adipose and fibroglandular regions for the examples considered in Fig. 1. This highlights the importance of tunning the regularization parameter and the need for developing regularization-free approaches such as the direct sensitivity approach.

The direct-sensitivity approach was effective in identifying the independent source-detector pairs for each region in imaging domain by considering the smallest direct-sensitivity coefficient (see Eq. (10)) which is mathematically equivalent to regularizing the solution by avoiding quantities with large magnitudes which could amplify the noise when multiplied with measurement vector, δY. On the other hand, the data-resolution approach requires the regularization parameter (λ) to estimate the data-resolution matrix (N) in Eq. (6). and further the optimal measurements are chosen based on the condition number of the matrix, N. The dependence of data-resolution matrix on these factors makes it less attractive for real-time or dynamic imaging where parameter-free approaches are preferred.

TABLE I
RMSE Calculated for the Cases Corresponding to Fig. 1

Case	Standard $\times 10^{-3}$	Data Resolution $\times 10^{-3}$	Proposed $\times 10^{-3}$
1	1.0	1.1	1.18
2	0.645	1.21	1.3
3	1.2	1.1	1.28
4	0.645	1.23	1.34
5	1.1	1.21	1.27
6	1.3	1.28	1.36
7	0.866	1.31	1.35

Case 1 to 7 refers to the reconstructed images starting from extreme left to right respectively.

The reconstruction results shown in Fig. 1 indicate the high-level data-optimization that could be obtained using the direct-sensitivity approach as opposed to the data resolution and standard approaches. The proposed scheme demanded only 3 measurements (fourth row) compared to the data resolution approach which resulted in requiring 6 measurements to quantify the absorption parameter. In order to investigate if the proposed scheme was biased to the target location in the imaging domain, various target location were considered resulting in seven different target locations to reconstruct the absorption parameter. This study showed the effectiveness of the proposed scheme to reconstruct the optical properties without requiring additional measurements irrespective of the target location. In order to quantify the reconstruction error associated with the standard, data resolution, and proposed methods with respect to the target distributions, the root mean square error (RMSE) metric was computed for all the seven cases considered. The RMSE in this case is defined as:

$$\text{RMSE} = \sqrt{\frac{1}{N}\sum_{i=1}^{N}(x^i_{\text{target}} - x^i_{\text{recon}})^2} \tag{13}$$

where x^i_{target} and x^i_{recon} are the target and reconstructed absorption (μ_a) values for the $i\text{th}$ region respectively, since there are three regions for the case considered here as a result $N = 3$. The RMSE was calculated for the reconstructed images corresponding to Fig. 1 and reported in Table I. It can be noted that the RMSE values obtained for the proposed scheme compared to the standard and data-resolution were in agreeable range. These errors can be further reduced if one considers more than one direct sensitivity coefficient (DSC) instead of the largest coefficient which was the case for all the studies performed in this work.

In order to quantify the role of μ_s' in the standard, data resolution, and proposed methods were illustrated in Fig. 2, and the corresponding RMSE for the for the case, $\mu_s' = 2\ \text{mm}^{-1}$ is 0.057, 0.0579, and 0.058 for the standard, data resolution and proposed approaches respectively, while the RMSE for the case

TABLE II
COMPARISON OF THE OPTIMAL MEASUREMENTS (M) REQUIRED FOR ALL THE RESULTS PRESENTED IN THIS WORK

Case	Standard	Data Resolution	Proposed
Patient Mimicking Experiment (Fig. 1)	240	6	3
Experimental Phantom (Fig. 2)	240	6	3
Human Breast Data (Fig. 3)	49	4	2

TABLE III
COMPUTATIONAL TIME (IN SECONDS) FOR THE RESULTS SHOWN IN THIS WORK

Case	Standard	Data Resolution	Proposed
Patient Mimicking Experiment (Fig. 1)	7.9 (6)	10.1 (15)	8.4 (70)
Experimental Phantom (Fig. 2)	9.2 (8)	11. 2 (7)	7.8 (55)
Human Breast Data (Fig. 3)	4.9 (4)	5.8 (7)	4.1 (33)

The total number of iterations taken for convergence is listed in parenthesis.

$\mu_s' = 1$ mm^{-1} is 0.001, 0.0011, and 0.00118 for the standard, data resolution and proposed approaches respectively. Note that the proposed and data resolution methods are less than 10% in error in comparison with the standard method for the results in Fig. 2. The error in estimation of μ_a stems from the fact that the reconstruction techniques models only for the changes in μ_a and not μ_s', therefore any changes in μ_s' is reflected in the μ_a (treated as unknown in all the cases). As a result, this numerical example demonstrates the robustness of the proposed method to estimate the μ_a distributions when there is a false assumption of μ_s'.

Next, a case of gelatin phantom data was considered to compare the proposed scheme with its counter parts results are as shown in Fig. 3. The results show that the proposed scheme performed on par with traditional and data resolution methods with only 3 minimal measurements while the data-resolution required 6 measurements. Finally, the utility of the proposed scheme in a real-time application was evaluated using a real human breast data and the corresponding results were shown in Fig. 4. In here, the purpose of this imaging was to quantify the small-scale pulsatile variations of hemoglobin inside the human breast. It is worth mentioning that this is a typical case of dynamic imaging where optimizing the source-detectors becomes very effective. The proposed scheme was utilized to identify the source-detector positions for each region (in this case 2) and the same source-detector pairs were utilized for the rest of the data-points to estimate the absorption parameter. The minimal number of source-detectors required by the proposed approach was only 2 while data resolution approach required 4 measurements. The source-detector positions are highlighted with symbols in Fig. 4. Further, the proposed scheme captured the small scale variations, which is in unison with the standard and data resolution approach although the amplitude recovered is less, however the phase and temporal delay had a close match with other schemes. This particular example demonstrates the reliability of the proposed scheme in capturing minute pulsatile variations in the human breast with minimal measurement requirement. In order to summarize the total source-detectors used in all the cases considered in this work, Table II compares the number of source detector pairs/ minimal measurements required for each case. Finally, the computational time was recorded for the results shown in this work. Table III summarizes the computational time in seconds with the number of iterations taken by the respective methods to reach the stopping criterion, given in parenthesis. The computation time taken for the proposed scheme reveals the fact that the time taken to estimate the solution for all the cases is relatively fast compared to its counter parts.The proposed scheme took many iterations to arrive at the final solution which is essentially due to the fact that the updates are very small and the large gap between the initial guess ($\mu_a = 0.01$) and the target ($\mu_a = 0.02$). However the time taken per iteration is extremely quick as there is no matrix building or inversion. In addition, the proposed scheme was found to be appropriate to reconstruct small updates effectively such as temporal variations in dynamic imaging (Fig. 4) with the advantage of measurement optimization. The implications of reducing measurements can be important in dynamic imaging scenarios where the geometry is fixed, as a result the proposed method can be utilized to calculate the optimal source-detector positions at the first time-point to establish a priori the required sources and detectors and the resulting configuration could be used for the consecutive time points (as demonstrated in the human breast data). This is potentially an advantage to reduce the complexity of instrumentation and reconstruction time. Finally, this work limited its discussion to 2D geometries, however the distinct advantage of reduction in the number of measurements using the proposed method compared to data resolution method can be more effective in 3D geometries, in which the data-collection configuration is typically more than three layers of sources-detectors planes resulting in a much lesser source-detector positions required by the proposed method in comparision with data resolution method .

VI. CONCLUSIONS

A direct-sensitivity approach was developed to optimize the data-collection procedure, which was free of heuristic parameters such as regularization or threshold parameters. The state-of-the-art measurement optimization (data resolution) scheme required a minimum of 2*R measurements (R being the number of distinct tissue regions), but in this work we proposed a direct sensitivity approach, which requires only R measurements. This was accomplished by identifying independent signal-to-noise data points and in-turn used this information to optimize the source detectors involved in acquiring the data. More importantly, the application of the direct sensitivity approach was found to be appropriate for dynamic imaging that involves small updates between successive data points was explored in this work using a real human breast data. The reconstruction algorithms that were developed as part of this work is available as an open-source for enthusiastic readers/users [22].

REFERENCES

[1] D. A. Boas *et al.*, "Imaging the body with diffuse optical tomography," *IEEE Signal Process. Mag.*, vol. 18, no. 6, pp. 57–75, Nov. 2001.

[2] S. Srinivasan *et al.*, "Interpreting hemoglobin and water concentration, oxygen saturation and scattering measured in vivo by near infrared breast tomography," *Proc. Nat. Acad. Sci USA*, vol. 100, pp. 12349–12354, 2003.
[3] J. C. Hebden *et al.*, "Three-dimensional optical tomography of the premature infant brain," *Phys. Med. Biol.*, vol. 47, pp. 4155–4166, 2002.
[4] S. R. Arridge and J. C. Schotland, "Optical tomography: Forward and inverse problems," *Inverse Probl.*, vol. 25, 2009, Art. no. 123010.
[5] A. H. Hielscher, A. D. Klose, and K. M. Hanson, "Gradient-based iterative image reconstruction scheme for time-resolved optical tomography," *IEEE Trans. Med. Imag.* vol. 18, no. 3, pp. 262–271, Mar. 1999.
[6] B. W. Pogue *et al.*, "Implicit and explicit prior information in near-infrared spectral imaging: Accuracy, quantification and diagnostic value," *Philos. Trans. A, Math. Phys. Eng. Sci.*, vol. 369, pp. 4531–4557, 2011.
[7] C. M. Carpenter *et al.*, "Image-guided optical spectroscopy provides molecular-specific information in vivo: MRI-guided spectroscopy of breast cancer hemoglobin, water, and scatterer size," *Opt. Lett.*, vol. 32, pp. 933–935, 2007.
[8] P. K. Yalavarthy *et al.*, "Structural information within regularization matrices improves near infrared diffuse optical tomography," *Opt. Express*, vol. 15, pp. 8043–8058, 2007.
[9] B. Brooksby, H. Dehghani, B. W. Pogue, and K. D. Paulsen, "Near-infrared (NIR) tomography breast image reconstruction with a priori structural information from MRI: Algorithm development for reconstructing heterogeneities," *IEEE J. Sel. Topics Quantum Electron.*, vol. 9, no. 2, pp. 199–209, Mar./Apr. 2003.
[10] B. Brooksby *et al.*, "Imaging breast adipose and fibro-glandular tissue molecular signatures using hybrid MRI-guided near-infrared spectral tomography," *Proc. Nat. Acad. Sci. USA*, vol. 103, pp. 8828–8833, 2006.
[11] J. P. Culver, V. Ntziachristos, M. J. Holboke, and A. G. Yodh, "Optimization of optode arrangements for diffuse optical tomography: A singular-value analysis," *Opt. Lett.*, vol. 26, pp. 701–703, 2001.
[12] P. K. Yalavarthy, H. Dehghani, B. W. Pogue, and K. D. Paulsen, "Critical computational aspects of near infrared circular tomographic imaging: Analysis of measurement number, mesh resolution and reconstruction basis," *Opt. Express*, vol. 14, pp. 6113–6127, 2006.
[13] L. Chen and N. Chen, "Optimization of source and detector configurations based on Cramer-Rao lower bound analysis," *J. Biomed. Opt.*, vol. 16, 2011, Art. no. 035001.
[14] J. Prakash and P. K. Yalavarthy, "Data-resolution based optimal choice of minimum required measurements for image-guided diffuse optical tomography," *Opt. Lett.*, vol. 38, pp. 88–90, 2013.
[15] D. Karkala and P. K. Yalavarthy, "Data-resolution based optimization of the data-collection strategy for near infrared diffuse optical tomography," *Med. Phys.*, vol. 39, pp. 4715–4725, 2012.
[16] J-P Morucci *et al.*, "A direct sensitivity matrix approach for fast reconstruction in electrical impedance tomography," *Physiol. Meas.*, vol. 15, 1994, Art. no. A107.
[17] J. P. Morucci, M. Granie, M. Lei, M. Chabert, and P. M. Marsili, "3D reconstruction in electrical impedance imaging using a direct sensitivity matrix approach," *Physiol. Meas.*, vol. 16, 1995, Art. no. A123.
[18] H. Dehghani *et al.*, "Near infrared optical tomography using NIRFAST: Algorithms for numerical model and image reconstruction algorithms," *Commun. Numer. Methods Eng.*, vol. 25, pp. 711–732, 2009.
[19] C. B. Shaw and P. K. Yalavarthy, "Effective contrast recovery in rapid dynamic near-infrared diffuse optical tomography using L1-norm-based linear image reconstruction method," *J. Biomed. Opt.*, vol. 17, pp. 086009:1–10, 2012.
[20] R. P. K. Jagannath and P. K. Yalavarthy, "An efficient gradient-free simplex method for estimation of optical properties in image-guided diffuse optical tomography," *J. Biomed. Opt.*, vol. 18, 2013, Art. no. 030503.
[21] Z. Li *et al.*, "Rapid magnetic resonance-guided near-infrared mapping to image pulsatile hemoglobin in the breast," *Opt. Lett.*, vol. 35, pp. 3964–3966, 2010.
[22] (2015). [Online]. Available: https://sites.google.com/site/sercmig/home/dsc

Calvin B. Shaw received the M.Sc and Ph.D. degrees in engineering from the Indian Institute of Science, Bangalore, in 2012 and 2014, respectively.

He is a Postdoctoral Research Scholar at the Department of Radiology and Radiological Science, Medical University of South Carolina, USA. His research interests include biomedical optics, photoacoustic imaging, inverse problems, diffusion MRI, diffusional kurtosis imaging, fiber tractography, and nueroimage analysis.

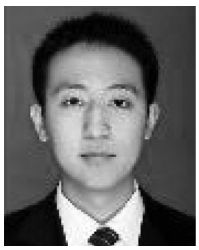

Zhiqiu Li received the M.E. degree from Tsinghua University, China, and the Ph.D. degree in biomedical engineering from Dartmouth College, Hanover, NH, USA, in 2011.

He is a Medical Physicist at the Vantage Oncology, Hospital and Health Care, Greater Los Angeles, USA. His research interests include MRI, radiation therapy, medical devices, brachytherapy, dosimetry, and clinical research.

Brian W. Pogue received the M.Sc. degree in physics from York University, Canada, and the Ph.D. degree in medical physics from McMaster University, Hamilton, ON, Canada, in 1996.

He is a Professor of engineering and physics & astronomy at the Thayer School of Engineering at Dartmouth, USA. His research interests include optics in medicine, biomedical imaging to guide cancer therapy; molecular guided surgery; dose imaging in radiation therapy; Cherenkov light imaging; image guided spectroscopy of cancer; modeling of tumor pathophysiology and contrast.

Phaneendra K. Yalavarthy received the M.Sc. degree in engineering from the Indian Institute of Science, Bangalore and the Ph.D. degree in biomedical computation from Dartmouth College, Hanover, NH, USA, in 2007.

He is an Associate Professor with the Department of Computational and Data Sciences at Indian Institute of Science, Bangalore. His research interests include medical image computing, medical image analysis, and biomedical optics.